communications materials

Article

https://doi.org/10.1038/s43246-024-00561-w

Positron unveiling high mobility graphene stack interfaces in Li-ion cathodes

Meiying Zheng [1,2], Jan Kuriplach[3], Ilja Makkonen [4], Rafael Ferragut [1,5] ✉, Vito Di Noto [6], Gioele Pagot[6], Ekaterina Laakso[7] & Bernardo Barbiellini [2,8,9] ✉

Carbon-based coatings in Li-ion battery cathodes improve electron conductivity and enable rapid charging. However, the mechanism is not well understood. Here, we address this question by using positrons as non-destructive probes to investigate nano-interfaces within cathodes. We calculate the positron annihilation lifetime in a graphene stack $LiCoO_2$ heterojunction using an ab initio method with a non-local density approximation to accurately describe the electron-positron correlation. This ideal heterostructure represents the standard carbon-based coating performed on cathode nanoparticles to improve the conduction properties of the cathode. We characterize the interface between $LiCoO_2$ and graphene as a p-type Schottky junction and find positron surface states. The intensity of the lifetime component for these positron surface states serves as a descriptor for positive ion ultra-fast mobility. Consequently, optimizing the carbon layer by enhancing this intensity and by analogizing Li-ion adatoms on graphene layers with positrons at surfaces can improve the design of fast-charging channels.

In commercial Lithium-ion batteries (LIBs)[1,2], active cathode microparticles are coated with the carbonaceous nano-layers to promote fast charging, by increasing electronic conductivity and preserving structural integrity[3–7]. Documented by G. Ceder et al.[8] and Q. Cao et al.[9], these layers are integral to improvements in charging and discharging rates. Designing the optimal electrode is a difficult task since the interstitial carbon-binder domains (CBD) composed of conductive additives affect the Li-ion transport within the nanocircuitry of $LiCoO_2$ (LCO) cathodes for LIBs[10]. In LCO, the redox reaction[11] governing the operation of the cathode can be written as follows $LiCoO_2 \leftrightarrow xLi^+ + Li_{(1-x)}CoO_2 + xe^-$. Upon charging, Li-ions and electrons leave the cathode and that is why transport properties are important. The presence of conventional carbon black in CBD leads to an increased tortuosity of the pore structure, thereby hindering the movement of Li-ions. The incorporation of graphene presents an ingenious solution[12] by reducing tortuosity, thus enhancing Li-ion diffusion.

By employing broadband electrical spectroscopy (BES), Pagot et al.[13] have taken a more fundamental and radical approach. They demonstrated that carbon coating plays a primary role independent of the electrolyte. Notably, unlike previous literature, their study investigated electrode materials before the addition of the electrolyte, avoiding this contribution. In this way, the authors focused solely on the interactions between the carbon matrix and lithium cobalt oxide microparticles. Their findings revealed that the addition of carbon results in a two-order-of-magnitude improvement in conductivity. Their experiments also show that using nanotubes leads to an additional two orders of magnitude improvement. These findings confirm that the ideal coating design should consider both electron and ion conduction pathways[14]. The study by Barone et al.[15] on the adsorption and diffusion of lithium atoms on graphene surfaces revealed the crucial role of Li adatoms in enabling rapid diffusion processes. Adatoms are defined as atoms that are adsorbed on the surface of a material. Upon trapping on a smooth carbon surface, the Li adatoms can easily move in multi-hopping processes[15] that allow fast charging to occur.

In the studies of positron trapping, quantum wells are often utilized to describe the trapping of positrons in copper quantum dots embedded in iron[16,17]. In our study, a lithium-deficient layer adjacent to the carbon layer presents a scenario similar to a quantum well. However, the positron affinity arguments utilized in the quantum well models, which are typically valid for metals, may not fully apply to heterojunctions involving semiconducting

[1]L-NESS and Department of Physics, Politecnico di Milano, Via Anzani 42, Como, IT-22100, Italy. [2]Department of Physics, School of Engineering Science, LUT University, Yliopistonkatu 34, Lappeenranta, FI-53851, Finland. [3]Department of Low Temperature Physics, Faculty of Mathematics and Physics, Charles University, V Holešovičkách 2, Prague, CZ-18000, Czech Republic. [4]Department of Physics, University of Helsinki, P.O. Box 43, Helsinki, FI-00014, Finland. [5]INFN Milano Unit, National Institute for Nuclear Physics, Via Celoria,16, Milan, IT-20133, Italy. [6]Section of Chemistry for the Technology (ChemTech), Department of Industrial Engineering, University of Padova, Via Marzolo 9, Padova, IT-35131, Italy. [7]Department of Separation Science, LUT University, Yliopistonkatu 34, Lappeenranta, FI-53851, Finland. [8]Department of Physics, Northeastern University, 360 Huntington Ave, Boston, MA, 02115, USA. [9]Quantum Materials and Sensing Institute, Northeastern University, Burlington, MA, 01803, USA. ✉e-mail: rafael.ferragut@polimi.it; bernardo.barbiellini@lut.fi

materials like LCO. In this work, by using fundamental laws of quantum mechanics manifested by highly accurate first-principles simulations, we demonstrate the existence of a positron trapped near a graphene stack (GS) interface in bulk LCO cathode with an energy comparable to Li sticking at the same surface. In this way, the positron acts as a light Li-ion analog. Therefore, once such a positron is trapped on a graphene surface inside the cathode, it indicates that some Li ions have followed a similar fate. Pagot et al.[13] suggested that positron annihilation spectroscopy (PAS) not only probes but also amplifies the detection of fast-moving Li adatoms within CBD structures inside cathodes of LIBs. Our study provides definitive proof of the role of the positron surface state as a quantum analog to investigate fast Li-ion mobility. To examine the positron surface state, we consider a simple yet highly realistic model of the bulk graphene interface at the surface of an LCO particle based on advanced two-component Density Functional Theory (TCDFT) for both electronic and positronic states.

Results and discussion

We consider an ideal graphene stack LCO heterostructure, denoted G ⊕ LCO. The optimized structures are illustrated in Fig. 1. Vacuum model (VC-G ⊕ LCO) is employed to represent the edge area of the core-shell graphene/LCO interface structure, while the sandwich model (SW-G ⊕ LCO) is utilized to simulate the bulk graphene/LCO nano interfaces. To examine the stability of our models, binding energy curves for the G ⊕ LCO heterostructures were calculated by using the Perdew–Burke–Ernzerhof (PBE)[18] with an additional Hubbard-type U term[19] (PBE+U) and Van der Waals (VdW) dispersion-correlation DFT-D3[20] functionals. The strength of the interlayer bonding between graphene layers and LCO crystal is estimated using the binding energy per surface given by $E_b = (E_{G⊕LCO} - E_{LCO} - E_G)/A$[21], where E_G and E_{LCO} are the total energies of the graphene, and the LCO components, respectively, and $E_{G⊕LCO}$ is the total energy of the G ⊕ LCO interface heterostructure. E_b as functions of the interlayer distance for G ⊕ LCO heterostructures is presented in Fig. 1e. A negative value of E_b indicates the energetic stability of the constructed heterostructures. Results also indicate that DFT-D3 functional VdW correction is necessary for both models, since PBE+U did not predict any stable heterostructure from the $E_b > 0$. It is worth noting that SW-G ⊕ LCO shows lower energy due to both C5 and C6 graphene layers bonding with the LCO surface. It is not surprising that the equilibrium distances in both systems are consistent at $d_1 = 2.4$ Å, suggesting the presence of comparable electrostatic ionic interactions between the C5 graphene layer and the LCO in both the SW and VC heterostructures. Our results of equilibrium distances exhibit reasonable agreement with previously reported values. Total-reflection high-energy positron diffraction (TRHEPD) determined a distance of 2.1 Å in the Graphene/metal (Co)[22], low energy electron diffraction (LEED) recorded 2.2 Å for Graphene/metal (Ni)[23], and normal incidence X-ray standing wave (NIXSW) identified 2.6 Å for Graphene/insulator (α-Al_2O_3)[24]. Furthermore, theoretical calculations with VdW corrections show the result of 2.1 Å for graphdiyne/LCO[25] and Graphene/Co[26], 2.6 Å for Graphene/Cr_2O_3 with an oxygen-termination model[27], and 2.9 Å for graphene/Cu[28], also support our findings. According to the results obtained at the equilibrium interlayer distances, SW-G ⊕ LCO displays a negative binding energy of −0.18 eV Å^{-2}, whereas VC-G ⊕ LCO exhibits a negative binding energy of −0.13 eV Å^{-2}, respectively.

Figure 2 shows the electronic band structure and the density of states (DOS) of SW-G ⊕ LCO at the equilibrium distance $d_1 = 2.4$ Å. Notably, the uncoated LCO slab exhibits a direct band gap of 2.63 eV (see Supplementary Fig. 1a), consistent with the experimental value of 2.5 eV[29]. However, after graphene is stacked with LCO, a metallic property emerges, predominantly due to the Dirac point of graphene shifts downward by 1.0 eV from the Fermi level (E_F) when compared to free-standing graphene (see Supplementary Fig. 1b), indicating charge transfer from LCO to the carbon layer.

Notably, as defined in ref. 30, the Schottky barrier height (SBH) for n-type or p-type can be described as the energy difference between the Fermi level (E_F) and the valence band maximum (E_V) or conduction band minimum (E_C), denoted as $\Phi_{Bn} = E_C - E_F$ or $\Phi_{Bp} = E_F - E_V$, as shown in Supplementary Fig. 2. An ohmic contact is established if either Φ_{Bp} or Φ_{Bn} holds a negative value. Besides, when $\Phi_{Bn} > \Phi_{Bp}$ indicates the formation of a p-type Schottky interface, otherwise it is an n-type interaction. Herein, Φ_{Bn} of LCO is predicted of 2.5 eV after coating, while the valence band maximum upon the Fermi level, with $\Phi_{Bp} = 0$ eV. This result provides a

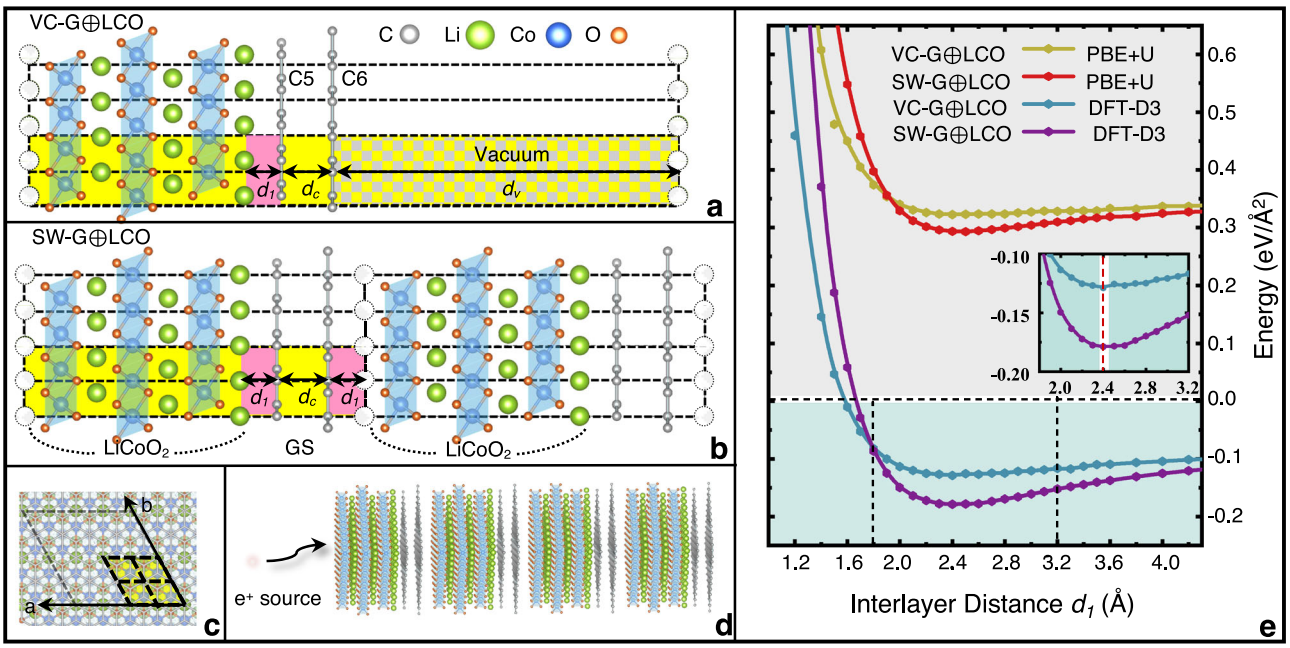

Fig. 1 | Two distinct schematic structures of graphene stack (GS) (001) $LiCoO_2$ (LCO) heterostructure. a Side view of the surface structure (vacuum model VC). **b** Side view of the buried interface structure (sandwich model SW). **c** Top view of SW and VC. **d** Schematic of positron injection into the SW supercell. **e** Binding energy with different interlayer distances of VC/SW-G ⊕ LCO heterostructures. Interlayer distance between carbon and $LiCoO_2$, two carbon layers are shown as d_1, d_c, respectively, while d_v indicates the vacuum distance in the VC model. The primitive cell is indicated by the black dashed lines, calculated supercells are shown in the yellow highlight area. The gray, green, blue, orange and white balls denote carbon, lithium, cobalt, oxygen, and missing lithium atoms, respectively.

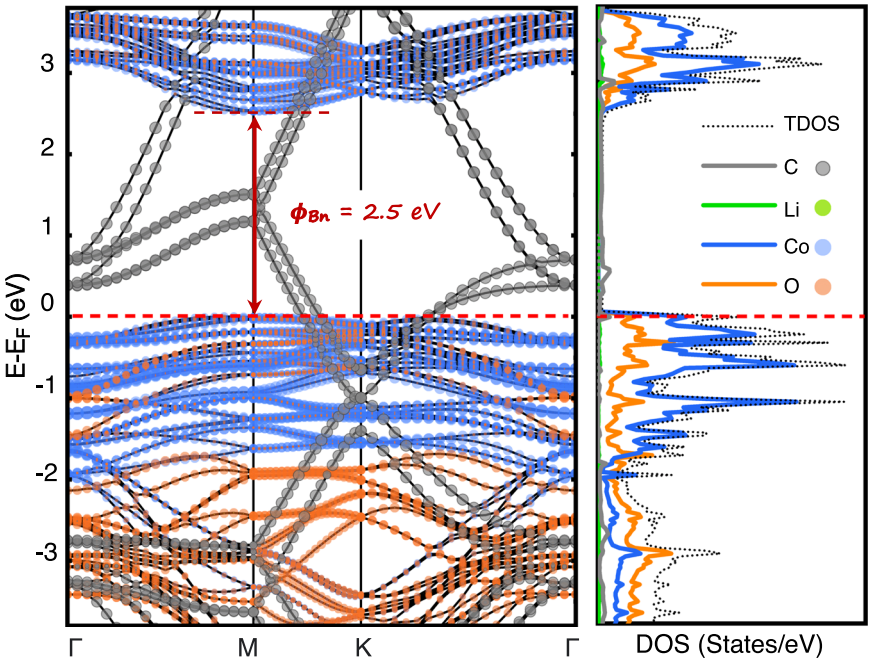

Fig. 2 | Electronic band structure and density of states (DOS) of SW-G ⊕ LCO at the equilibrium distance $d_1 = 2.4$ Å. Total electronic states, C, Li, Co, and O, are shown in black dashed lines, gray, lime green, blue, and orange, respectively. High symmetry lines are calculated along Γ, M, K, Γ. Dirac point of graphene is located at the *K*-point and shifts downward by 1.0 eV with respect to the Fermi level shown in the red dashed line.

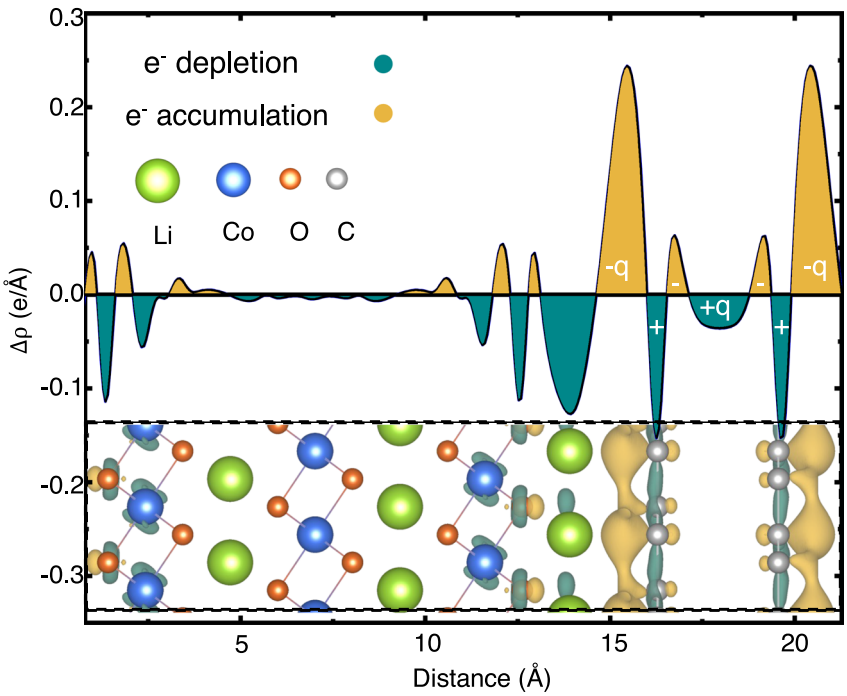

Fig. 3 | Calculated plane-averaged charge density difference of SW-G ⊕ LCO perpendicular to (001) plane at the equilibrium distance. The corresponding isosurface of charge density difference is the inset. Orange (green) region represents charge accumulation (depletion). The interlayer dipole moment per surface area is 0.14 D Å^{-1}. The isosurface value is 0.0016 e Å^{-3}.

reasonable explanation for the open question posed in our previous experimental work[13]. Our DFT calculations confirm the interaction type between carbon and LCO interface identity as a p-type Schottky Junction rather than an ohmic contact.

To understand the long-range electron exchange process, we display the plane-averaged charge difference parallel to the interface between GS and LCO, shown in Fig. 3. The charge density difference is defined as $\Delta\rho = \rho_{\rho_{G\oplus LCO}} - \rho_{LCO} - \rho_G$, where $\rho_{G\oplus LCO}$, ρ_{LCO}, ρ_G are the charge densities of G ⊕ LCO, LCO, and graphene layers, respectively. From Fig. 3, it is evident that the charge transfer process due to the heterojunction construction is predominantly localized at the bulk interfaces, leading to electron charge depletion near the lithium-terminated interlayer. In contrast, the graphene surfaces exhibit an electron charge density accumulation area, consistent with our earlier electronic band structure analysis. Consequently, a surface dipole per unit area forms at the GS and LCO interface. The Schottky barrier height is influenced by this interface dipole, primarily due to the charge transfer process occurring in the absence of external electric fields[30]. The physical explanation for this dipole formation is that electron displacement induced the carbon hole doping, leading to a negative charge region ($-q$), where the subtle electrostatic field effect can occur[31].

The properties of positrons in LCO can be reliably calculated through DFT by using weighted density approximation (WDA) functional and

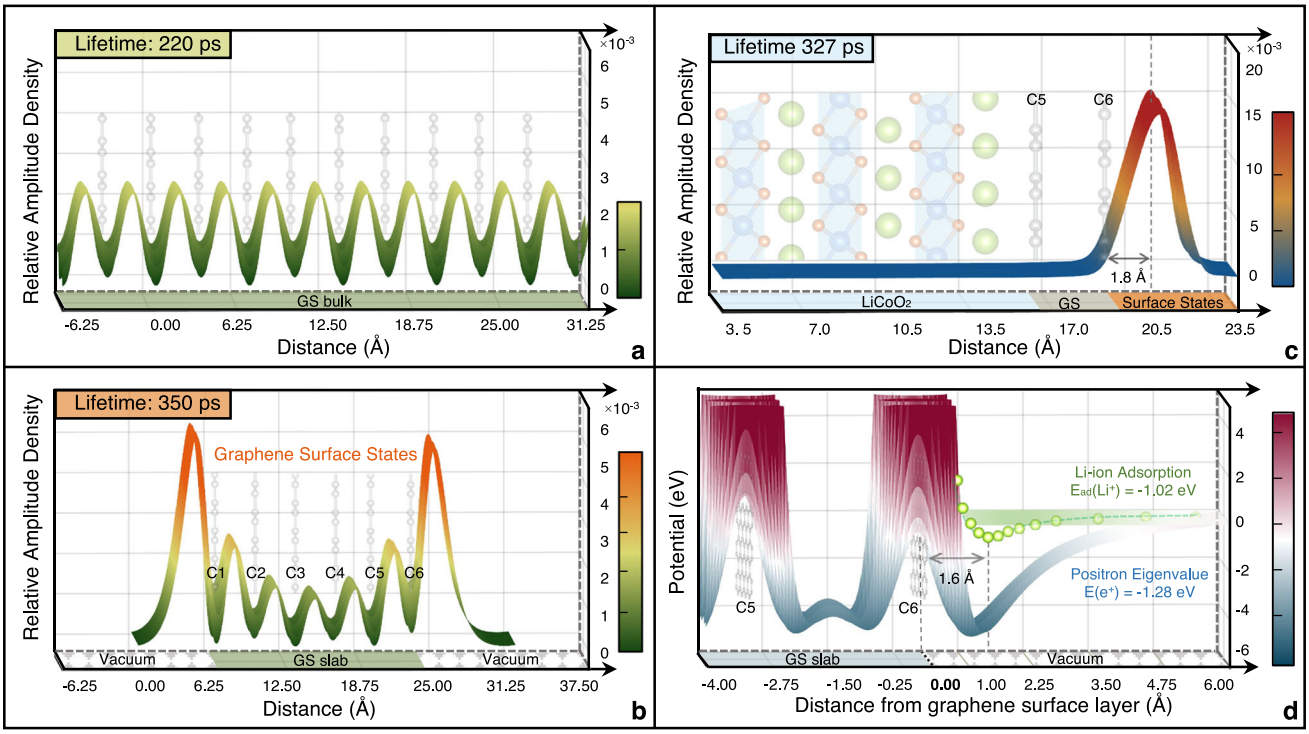

Fig. 4 | Results of the positron calculations. a Graphene stack (GS) bulk. **b** Six-layer GS slab. **c** SW-G ⊕ LCO heterostructure. The maximum positron probability density occurs at 1.8 Å from the graphene surface. Ground-state positron densities are presented along the *c* direction. **d** Three-dimensional plot of calculated WDA positron total potential in a GS slab. The positron eigenvalue with respect to the vacuum level is −1.28 eV. DFT calculated energies of Li-ion adsorption on the graphene surface are shown in green circles. The stable adsorption site is located at 1.6 Å near the C6 surface with a coordination energy of −1.02 eV. The primary mechanisms in carbon–positron and carbon–lithium interactions are electron–positron correlation effects and Van der Waals interactions, respectively.

correspond to the first-lifetime component identified in the positron annihilation experiment performed by Pagot et al.[13]. However, the second component lifetime above 300 ps measured by these authors have not been explained from the first-principles in previous papers. Here we bridge this gap in knowledge. Our main results are shown in Fig. 4 and demonstrate that the second-lifetime component originates from a positron surface state on a GS interface. Figure 4a corresponds to a positron state inside GS bulk, typically referred to as graphite, with a calculated lifetime below 300 ps. Therefore, one can conclude that the experimental second component lifetime does not correspond to GS bulk. In contrast, in the cases of Fig. 4b six-layer GS slab and Fig. 4c SW-G ⊕ LCO heterostructure, the calculated lifetime exceeds 300 ps, aligning with the experiment. Compared to the GS slab model, which exhibits the double-sided edge effects, the SW model demonstrates surface states primarily at the interface between the C6 graphene surface and the oxygen-terminated layer. As a result, the SW model has a shorter lifetime than the GS slab. This is due to enhanced positron confinement at the lithium-depleted layer, which leads to more rapid annihilation events and, consequently, shorter lifetimes. The agreement between theoretical and experimental values indicates that a positron surface state can explain the experimental value of the second-lifetime component.

We now discuss the similarity between the Li adatoms and positron surface states on graphene. The Li adsorption energy on the GS surface E_{ad}(Li) is calculated by using

$$E_{ad}(\mathrm{Li}) = E_{tot}(\mathrm{Li} \oplus \mathrm{G}) - E_{iso}(\mathrm{Li}) - E_{tot}(\mathrm{G}), \quad (1)$$

where E_{iso}(Li) is the isolated lithium ion, E_{tot}(Li ⊕ G) and E_{tot}(G) represent the total energies of the lithium-adsorped graphene system and pristine graphene, respectively. We confirm that the most stable coordination site is at 1.6 Å from the graphene surface, with an adsorption energy of about −1.02 eV in good agreement with previously reported values of 1.8 Å (−1.06 eV)[32], 1.44 Å (−1.46 eV)[33], 1.52 Å (−1.69 eV)[34], respectively. Particularly, the maximum positron density of Fig. 4c (see Supplementary Fig. 3) is located at about 1.8 Å, which compares well with the Li adatom equilibrium positions. Moreover, Fig. 4d shows the comparison of the positron potential to the lithium adsorption energy E_{ad}(Li). As expected, the two curves show similar behaviour, and the positron eigenvalue with respect to the vacuum level is −1.28 eV. Therefore, we can conclude that the positron surface state is the analogue as of the Li-adatom sticking on the graphene surface. Notably, the observed discrepancy of ~0.4 eV in the surface state binding energy of graphene between the theoretical calculation and experimental results may be attributed to the presence of defects in the real surface. Also, positron surface binding energies vary with changes in surface atomic structure and electron density, as well as with surface reconstruction[35,36].

Another possible analogue of the Li-ion is the positive muon (μ^+), known to experience similar potentials as positrons, which also tends to localize in empty spaces[37]. This elementary particle is already routinely used as a battery probe, and McClelland et al.[38] have reviewed how positive muon spin relaxation (μSR) spectroscopy is employed to study ion diffusion in various battery materials. These authors have reported typical lithium diffusion coefficient values in active cathode materials ranging from 10^{-10} to 10^{-12} cm^2 s^{-1}, and similar values have been detected in Johnston et al.'s work[39]. Notably, the BES study detects fast mobilities, and the PAS study indicates the pathway using positron lifetime in the cathode LCO/C samples, with a Li-ion diffusion coefficient between 10^{-7} and 10^{-9} cm^2 s^{-1}[13]. The Li adatom and positron surface states correspondence shown in this work allow us to conclude that these new results can be assigned to Li adatoms[15] moving on smooth carbon layers such as graphene, which form fast highways for Li ions within the cathode nano circuitry[40]. Combined BES and PAS experiments also observed that the concentration of mobile Li ions in the fast diffusion channels of the cathodes is 1%, while the fraction of positrons in these same locations outside the cathode LCO material is

26–41%, given by the intensity I_2. Positron lifetime for the surface state on carbon can determine the parameters α and β in the linear combination of the LCO/C Doppler profile contributions, as demonstrated by Pagot et al.[13]. Consequently, we deduce that PAS amplifies the BES signal given by the mobile Li-ion concentration. This phenomenon is easily understandable, given the substantial mass difference between the positron and the Li-ion, together with the quantum mechanical nature of the positron, which aids in rapidly identifying fast pathways for positive ions.

Conclusions

We have shown that the interface between $LiCoO_2$ and graphene forms a p-type Schottky junction. Our findings also confirm the existence of a positron surface state, serving as the quantum counterpart to a classical Li adatom on the GS LCO interface. This unique positron state functions as a precise probe for identifying Li-ion fast highways along buried GS LCO interfaces within the Li-ion battery cathode. Our method enables the identification of ultra-fast channels for Li diffusion within the active cathode microcrystals. The intensity linked to the positron surface state lifetime provides an amplified signal reflecting the concentration of Li fast-moving adatoms detected by BES. This innovative approach allows the assessment of electrode performance. Our studies without liquid electrolytes not only introduce a novel direction for the technological advancement of ultrafast batteries but also ensure the applicability of our conclusions to lithium-ion solid-state batteries since solid electrolytes do not penetrate the cathode materials. A comprehensive understanding of the intricacies at the buried interfaces of the cathode material is imperative for enhancing conventional LIBs and propelling the development of next-generation solid-state batteries.

Methods

Vienna ab initio simulation package (VASP) calculations

We calculate the electronic ground state by using a first-principles method, as implemented in the Vienna ab initio simulation package (VASP)[41]. The projector augmented wave (PAW)[42] basis and the Perdew–Burke–Ernzerhof (PBE)[18] exchange-correlation energy functional within the generalized gradient approximation (GGA)[43] were employed in the relaxations. To address the on-site Coulombic interactions in the localized d electrons of Co ions, the GGA + U method[19] with an additional Hubbard-type U term (with a U–J value of 3.3 eV)[44] was applied. A cutoff energy of 600 eV and a Γ-centered Monkhorst–Pack $9 \times 9 \times 1$ k-mesh[45] with a 0.2 eV Gaussian smearing were utilized. The hexagonal cell with $a = 5.6$ Å is shown in Fig. 1c. The convergence criterion was 10^{-4} eV for total energy, and the valence electrons were treated as the Li-2s, Co-3d4s, O-2s2p, C-2s2p electrons. Surfaces in the vacuum model were set in a slab with the vacuum region no < 20 Å along the c-direction (perpendicular to the interface) to avoid interactions between the periodic images. We utilize the DFT-D3 method[20] with VdW-dispersion correction to predict stable heterostructures, effectively capturing the interactions of weakly bonded layers that critically influence binding energies. The equilibrium interlayer distance of graphene with AB stacking is fixed as d_c of 3.30 Å[46], while the interlayer distance between the carbon and lithium layers is presented as a variable d_1 changing from 0.8 to 5.0 Å.

Two components density functional theory (TCDFT)

In order to calculate the positron annihilation characteristics, we employ two components density functional theory (TCDFT)[47,48] with zero positron density limit. Using this computing scheme, we calculate the positron wave function, where the positron potential is given by the sum of the Coulomb potential and the electron-positron correlation potential. Concerning this last contribution of the potential for solid bulk materials, Boroński–Nieminen local density approximation (LDA)[47] and parameter-free GGA[49] provide reliable results. As shown in Table 1, the GS bulk LDA and GGA lifetimes are predicted to be 187, 200 ps, respectively. Remarkably, these values align with the previous atomic superposition Boroński-Nieminen LDA lifetime calculated as 204 ps and experimental value of 208 ps[50]. Moreover, for the LCO bulk lifetime, our LDA and GGA calculations indicate lifetime values of 120, 129 ps, respectively. These results are consistent with prior parameter-free GGA positron lifetime calculations of 131 ps[51] and correspond to the first-lifetime component identified in the positron annihilation experiment performed by Pagot et al.[13]. The slightly higher experimental value 145 ps can be explained by the presence of few Li vacancy in the LCO crystal.

Table 1 | Positron lifetime components

	TCDFT (ps)			Exp (ps)
Samples	LDA	GGA	WDA	
GS bulk	187	200	220	208[50]
LCO bulk	120	129	136	145[13]
GS slab	451	491	350	/
G ⊕ LCO	240	280	327	319–332[13]

However, when applied to the surface, these standard (semi-)local approximations fail to describe the image potential outside the surface[52]. Non-local approaches such as weighted density approximation (WDA)[53–56] are important for obtaining the correlation effects arising from the complex clouds present at surfaces and interfaces. The positron calculation results for G ⊕ LCO heterostructure are also illustrated in Supplementary Fig. 3. While all three methods produce similar positron wavefunctions upon solving the three-dimensional Schrödinger equation for the positron, the WDA method predicts a surface state lifetime of 327 ps. Since the lifetime values are obtained from the inverse of the annihilation rate, the enhancement factor γ is the key to predicting reliable results. The lifetime of 350 ps specifically reflects the ground state of the 6-layer GS slab model using the WDA approximation; it does not represent a linear combination of the bulk state and surface state. Our theoretical predictions align with the range of lifetime values from 319 to 347 ps observed in PAS measurements by Pagot et al.[13], performed on the cathodes without electrolyte. Notably, P. Parz et al.[57] reported PAS experiments on carbon black (Super P)-coated LCO cathodes, indicating a different scenario when the liquid electrolyte is involved. Moreover, their PALS analysis[57] utilized a different criterion for subtracting the Al contribution, as discussed by Pagot et al.[58]. However, the lifetime result of 206 ps[57] for fully lithium-loaded cathodes aligns with the average positron lifetime of 232 ps calculated in our work.

The electron-positron enhancement factor γ is a crucial component to calculate the annihilation rate λ and the positron lifetime τ[47,48] given for the LDA case by

$$\lambda = \frac{1}{\tau} = \pi r_e^2 c \int d\mathbf{r}\, n_e(\mathbf{r})\, n_p(\mathbf{r}) \gamma(n_e(\mathbf{r})), \tag{2}$$

where r_e is the classical electron radius, c is the speed of light, $n_e(\mathbf{r})$ and $n_p(\mathbf{r})$ are, respectively, the electron and the positron density. In the WDA, the local density is replaced by the total effective density $\widetilde{n}_e(\mathbf{r})$.

$$\widetilde{n}_e(\mathbf{r}) = n_{e,c}(\mathbf{r}) + n^*_{e,v}(\mathbf{r}), \tag{3}$$

where $n_{e,c}(\mathbf{r})$ is the core electron density and $n^*_{e,v}(\mathbf{r})$ is an effective valence electron density, a method known as the shell-partitioning scheme. Positron lifetimes are then given by

$$\lambda = \frac{1}{\tau} = \pi r_e^2 c \int d\mathbf{r}\, n_e(\mathbf{r})\, n_p(\mathbf{r}) \gamma(n_{e,c}(\mathbf{r}) + n^*_{e,v}(\mathbf{r})). \tag{4}$$

All the lifetimes mentioned in the main part are based on WDA, and we use the screening charge $Q = 1.0$ to determine the effective electron density by solving the modified sum rule described in ref. 54.

Data availability

The data that support the findings of this study are available from the corresponding author upon reasonable request.

Received: 7 February 2024; Accepted: 1 July 2024;
Published online: 27 July 2024

References

1. Tarascon, J.-M. & Armand, M. Issues and challenges facing rechargeable lithium batteries. *Nature* **414**, 359–367 (2001).
2. Goodenough, J. B. & Park, K.-S. The Li-ion rechargeable battery: a perspective. *J. Am. Chem. Soc.* **135**, 1167–1176 (2013).
3. Sim, S.-J., Lee, S.-H., Jin, B.-S. & Kim, H.-S. Use of carbon coating on $LiNi_{0.8}Co_{0.1}Mn_{0.1}O_2$ cathode material for enhanced performances of lithium-ion batteries. *Sci. Rep.* **10**, 11114 (2020).
4. Deng, S. et al. Boosting fast energy storage by synergistic engineering of carbon and deficiency. *Nat. Commun.* **11**, 132 (2020).
5. Li, P., Zhang, K. & Park, J. H. Dual or multi carbonaceous coating strategies for next-generation batteries. *J. Mater. Chem. A* **6**, 1900–1914 (2018).
6. Yoon, H. et al. Chloroaluminate anion intercalation in graphene and graphite: from two-dimensional devices to aluminum-ion batteries. *Nano Lett.* **22**, 1726–1733 (2022).
7. Zhao, H. et al. Learning heterogeneous reaction kinetics from x-ray videos pixel by pixel. *Nature* **621**, 289–294 (2023).
8. Kang, B. & Ceder, G. Battery materials for ultrafast charging and discharging. *Nature* **458**, 190–193 (2009).
9. Cao, Q. et al. A novel carbon-coated licoo2 as cathode material for lithium ion battery. *Electrochem. Commun.* **9**, 1228–1232 (2007).
10. Kroll, M. et al. Three-phase reconstruction reveals how the microscopic structure of the carbon-binder domain affects ion transport in lithium-ion batteries. *Batter. Supercaps* **4**, 1363–1373 (2021).
11. Shang, T. et al. Real-space measurement of orbital electron populations for $Li_{1-x}CoO_2$. *Nat. Commun.* **13**, 5810 (2022).
12. Chi, T. et al. Unraveling the effect of conductive additives on Li-ion diffusion using electrochemical impedance spectroscopy: a case study of graphene vs. carbon black. *J. Electrochem. Soc.* **170**, 040515 (2023).
13. Pagot, G. et al. Quantum view of Li-ion high mobility at carbon-coated cathode interfaces. *iScience* **26**, 105794 (2023).
14. Wei, W. et al. The effect of graphene wrapping on the performance of life PO_4 for a lithium ion battery. *Carbon* **57**, 530–533 (2013).
15. Uthaisar, C. & Barone, V. Edge effects on the characteristics of Li diffusion in graphene. *Nano Lett.* **10**, 2838–2842 (2010).
16. Nagai, Y. et al. Positron confinement in ultrafine embedded particles: quantum-dot-like state in an Fe–Cu alloy. *Phys. Rev. B* **61**, 6574 (2000).
17. Fazleev, N., Nadesalingam, M. & Weiss, A. Studies of positrons trapped at quantum-dot like particles embedded in metal surfaces. *AIP Conf. Proc.* **1099**, 956–959 (2009).
18. Perdew, J. P. et al. Restoring the density-gradient expansion for exchange in solids and surfaces. *Phys. Rev. Lett.* **100**, 136406 (2008).
19. Jain, A. et al. Formation enthalpies by mixing gga and gga+u calculations. *Phys. Rev. B* **84**, 045115 (2011).
20. Grimme, S., Antony, J., Ehrlich, S. & Krieg, H. A consistent and accurate ab initio parametrization of density functional dispersion correction (DFT-D) for the 94 elements H-Pu. *J. Chem. Phys*. **132**, (2010).
21. Yu, J. et al. High-performance borophene/graphene heterostructure anode of lithium-ion batteries achieved via controlled interlayer spacing. *ACS Appl. Energy Mater.* **3**, 11699–11705 (2020).
22. Fukaya, Y., Entani, S. & Sakai, S. Reversible structure change in graphene/metal interface by intercalation and deintercalation. *Phys. Rev. B* **108**, 155422 (2023).
23. Gamo, Y., Nagashima, A., Wakabayashi, M., Terai, M. & Oshima, C. Atomic structure of monolayer graphite formed on Ni (111). *Surf. Sci.* **374**, 61–64 (1997).
24. Entani, S. et al. Contracted interlayer distance in graphene/sapphire heterostructure. *Nano Res.* **8**, 1535–1545 (2015).
25. Gong, S., Wang, S., Liu, J., Guo, Y. & Wang, Q. Graphdiyne as an ideal monolayer coating material for lithium-ion battery cathodes with ultralow areal density and ultrafast Li penetration. *J. Mater. Chem. A* **6**, 12630–12636 (2018).
26. Vanin, M. et al. Graphene on metals: a van der Waals density functional study. *Phys. Rev. B* **81**, 081408 (2010).
27. Hou, X., Wumiti, M., Kumar, S., Shimada, K. & Sawada, M. Observation of mid-gap states emerging in the o-terminated interface of Cr_2O_3/graphene: a combined study of ab initio prediction and photoemission analysis. *Appl. Surf. Sci.* **594**, 153416 (2022).
28. Hamada, I. & Otani, M. Comparative van der Waals density-functional study of graphene on metal surfaces. *Phys. Rev. B* **82**, 153412 (2010).
29. Rosolen, J. M. & Decker, F. Photoelectrochemical behavior of $LiCoO_2$ membrane electrode. *J. Electroanal. Chem.* **501**, 253–259 (2001).
30. Qin, X., Hu, W. & Yang, J. Tunable Schottky and ohmic contacts in graphene and tellurene van der Waals heterostructures. *Phys. Chem. Chem. Phys.* **21**, 23611–23619 (2019).
31. Di Bartolomeo, A. Graphene Schottky diodes: an experimental review of the rectifying graphene/semiconductor heterojunction. *Phys. Rep.* **606**, 1–58 (2016).
32. Allouche, A. & Krstic, P. S. Atomic hydrogen adsorption on lithium-doped graphite surfaces. *Carbon* **50**, 510–517 (2012).
33. Fan, X., Zheng, W., Kuo, J.-L. & Singh, D. J. Adsorption of single li and the formation of small li clusters on graphene for the anode of lithium-ion batteries. *ACS Appl. Mater. interfaces* **5**, 7793–7797 (2013).
34. Yao, F. et al. Diffusion mechanism of lithium ion through basal plane of layered graphene. *J. Am. Chem. Soc.* **134**, 8646–8654 (2012).
35. Fairchild, A. J. et al. Photoemission spectroscopy using virtual photons emitted by positron sticking: a complementary probe for top-layer surface electronic structures. *Phys. Rev. Lett.* **129**, 106801 (2022).
36. Fazleev, N. Surface states and annihilation characteristics of positrons trapped at reconstructed semiconductor surfaces. *Appl. Surf. Sci.* **252**, 3333–3341 (2006).
37. Antognini, A. et al. Muonium emission into vacuum from mesoporous thin films at cryogenic temperatures. *Phys. Rev. Lett.* **108**, 143401 (2012).
38. McClelland, I. et al. Muon spectroscopy for investigating diffusion in energy storage materials. *Annu. Rev. Mater. Res.* **50**, 371–393 (2020).
39. Johnston, B. I., McClelland, I., Baker, P. J. & Cussen, S. A. Elucidating local diffusion dynamics in nickel-rich layered oxide cathodes. *Phys. Chem. Chem. Phys.* **25**, 25728–25733 (2023).
40. Zhu, C., Usiskin, R. E., Yu, Y. & Maier, J. The nanoscale circuitry of battery electrodes. *Science* **358**, eaao2808 (2017).
41. Kresse, G. & Furthmüller, J. Efficient iterative schemes for ab initio total-energy calculations using a plane-wave basis set. *Phys. Rev. B* **54**, 11169 (1996).
42. Blöchl, P. E. Projector augmented-wave method. *Phys. Rev. B* **50**, 17953 (1994).
43. Perdew, J. P., Burke, K. & Ernzerhof, M. Generalized gradient approximation made simple. *Phys. Rev. Lett.* **77**, 3865 (1996).
44. Wang, L., Maxisch, T. & Ceder, G. Oxidation energies of transition metal oxides within the GGA+ u framework. *Phys. Rev. B* **73**, 195107 (2006).
45. Bende, D., Wagner, F. R., Sichevych, O. & Grin, Y. Chemical bonding analysis as a guide for the preparation of new compounds: the case of VIrGe and HfPtGe. *Angew. Chem. Int. Ed.* **129**, 1333–1338 (2017).
46. Spanu, L., Sorella, S. & Galli, G. Nature and strength of interlayer binding in graphite. *Phys. Rev. Lett.* **103**, 196401 (2009).
47. Boroński, E. & Nieminen, R. Electron–positron density-functional theory. *Phys. Rev. B* **34**, 3820 (1986).
48. Puska, M. J. & Nieminen, R. M. Theory of positrons in solids and on solid surfaces. *Rev. Mod. Phys.* **66**, 841 (1994).
49. Barbiellini, B. & Kuriplach, J. Proposed parameter-free model for interpreting the measured positron annihilation spectra of materials

using a generalized gradient approximation. *Phys. Rev. Lett.* **114**, 147401 (2015).
50. Onitsuka, T., Ohkubo, H., Takenaka, M., Tsukuda, N. & Kuramoto, E. Positron lifetime calculation for defects and defect clusters in graphite. *J. Nucl. Mater.* **283**, 922–926 (2000).
51. Barbiellini, B. & Kuriplach, J. Improved generalized gradient approximation for positron states in solids. *J. Phys. Conf. Ser*. **791**, 012016 (2017).
52. Nieminen, R. M. & Puska, M. J. Positron surface states on clean and oxidized al and in surface vacancies. *Phys. Rev. Lett.* **50**, 281 (1983).
53. Rubaszek, A. Electron-positron enhancement factors at a metal surface: aluminum. *Phys. Rev. B* **44**, 10857 (1991).
54. Callewaert, V., Saniz, R., Barbiellini, B., Bansil, A. & Partoens, B. Application of the weighted-density approximation to the accurate description of electron–positron correlation effects in materials. *Phys. Rev. B* **96**, 085135 (2017).
55. Shi, W. et al. Nature of the positron state in CdSe quantum dots. *Phys. Rev. Lett.* **121**, 057401 (2018).
56. Chirayath, V. et al. Auger electron emission initiated by the creation of valence-band holes in graphene by positron annihilation. *Nat. Commun.* **8**, 16116 (2017).
57. Parz, P. et al. Charging-induced defect formation in Li_xCoO_2 battery cathodes studied by positron annihilation spectroscopy. *Appl. Phys. Lett.* **102**, 151901 (2013).
58. Pagot, G., Toso, V., Barbiellini, B., Ferragut, R. & Di Noto, V. Positron annihilation spectroscopy as a diagnostic tool for the study of $LiCoO_2$ cathode of lithium-ion batteries. *Condens. Matter* **6**, 28 (2021).

Acknowledgements

Enlightening discussions with A. Weiss is appreciated. M.Z. gratefully acknowledges a grant from the China Scholarship Council (CSC). This research was also supported by the Ministry of Education and Culture (Finland), Politecnico di Milano (Italy), and the LUT INERCOM Platform. The authors acknowledge the CSC—IT Center for Science, Finland, for computer time and the ELMO-LION doctoral summer school funded by EIT Raw Materials for educational resources. J.K. acknowledges the support from the Ministry of Education, Youth and Sports of the Czech Republic through the e-INFRA CZ (ID:90254). The work at Padova University was supported by the program "Budget Integrato per la Ricerca Inter-dipartimentale - BIRD 2021" of the University of Padova (project ACHILLES, protocol number BIRD219831).

Author contributions

DFT calculations, Meiying Zheng (M.Z.), Jan Kuriplach (J.K.), Ilja Makkonen (I.M.), Bernardo Barbiellini (B.B.); Comparison with experiments, Rafael Ferragut (R.F.), Vito Di Noto (V.D.N.), Gioele Pagot (G.P.), Ekaterina Laakso (E.L.). All authors have participated in the writing of the manuscript.

Competing interests

The authors declare no competing interests.

Additional information

Supplementary information The online version contains supplementary material available at https://doi.org/10.1038/s43246-024-00561-w.

Correspondence and requests for materials should be addressed to Rafael Ferragut or Bernardo Barbiellini.

Peer review information *Communications Materials* thanks V.A. Chirayath, Lu Feng and the other, anonymous, reviewer(s) for their contribution to the peer review of this work. Primary Handling Editors: Jet-Sing Lee. A peer review file is available.